www.advenergymat.de

Unraveling the Role of Surficial Oxygen Vacancies in Stabilizing Li-Rich Layered Oxides

Kai Wang, Jimin Qiu, Fuchen Hou, Ming Yang, Kaiqi Nie, Jiaou Wang, Yichao Hou, Weiyuan Huang, Wenguang Zhao, Peixin Zhang, Junhao Lin, Jiangtao Hu,* Feng Pan,* and Mingjian Zhang*

Li-rich layered oxides based on the anionic redox chemistry provide the highest practical capacity among all transition metal (TM) oxide cathodes but still struggle with poor cycling stability. Here, a certain amount of oxygen vacancies (OVs) are introduced into the ≈ 10 nm-thick surface region of $\rm Li_{1.2}Ni_{0.13}Co_{0.13}Mn_{0.54}O_2$ through a long-time medium-temperature post-annealing. These surficial enriched OVs significantly suppress the generation of O-O dimers ($\rm O_2^{n-}$, 0 < n < 4) and the associated side reactions, thus facilitating the construction of a uniform and compact cathode/electrolyte interphase (CEI) layer on the surface. The CEI layer then decreases the further side reactions and TM dissolution and protects the bulk structure upon cycling, eventually leading to enhanced cycling stability, demonstrated in both half cells and full cells. An in-depth understanding of OVs is expected to benefit the design of stable cathode materials based on anionic redox chemistry.

1. Introduction

There is an urgent need for cathodes with high specific energy to meet the requirements of fast-growing electric vehicles (EVs). Benefitting from the cooperative contribution of transition metal (TM) redox and oxygen redox, Li-rich layered oxide cathodes (LROs) with high theoretical specific capacity (>300 mA h g $^{-1}$)[2]

are promising candidates for the next generation high-energy-density lithiumion batteries. However, limited by the poor reversibility of lattice oxygen redox, LROs suffer from grievous oxygen release, TM ions migration and phase degradation from layered to spinel and finally to rock-salt phase (L-S-R), eventually resulting in battery failure and even safety hazards.

In previous studies, as the product of lattice oxygen loss upon cycling, oxygen vacancies (OVs) gave the notorious impression that pernicious to structural stability and electrochemical performance. The OVs are thought to be closely related to cation mixing,^[6] cation migration from TM layers to Li layers,^[7] L-S-R phase transition,^[8] sharp shrinking of

the cell volume,^[9] and even the formation of the nanopores in the bulk lattice.^[10] Recently, the positive roles of intrinsic OVs formed during synthesis were detected such as suppressing structural degradation,^[11] affecting local Mn coordination environments,^[12] decreasing the density of states of the O 2p band for reversible oxygen redox process,^[13] and inhibiting the significant voltage decay.^[14] Nevertheless, the understanding of

K. Wang, J. Qiu, W. Huang, W. Zhao, F. Pan School of Advanced Materials Peking University Shenzhen Graduate School Shenzhen, Guangdong 518055, P. R. China E-mail: panfeng@pkusz.edu.cn F. Hou, J. Lin Department of Physics Southern University of Science and Technology Shenzhen, Guangdong 518055, P. R. China M. Yang, P. Zhang, J. Hu College of Chemistry and Environmental Engineering Shenzhen University Shenzhen, Guangdong 518060, P. R. China E-mail: hujt@szu.edu.cn

Institute of High Energy Physics
Chinese Academy of Sciences
Beijing 100049, P. R. China
Y. Hou
State Key Laboratory of Applied Organic Chemistry
Key Laboratory of Nonferrous Metal Chemistry
and Resources Utilization of Gansu Province
Frontiers, Science Center for Rare Isotopes
College of Chemistry and Chemical Engineering
Lanzhou University
Lanzhou, Gansu 730000, P. R. China
M. Zhang
School of Science and Engineering
The Chinese University of Hong Kong
Shenzhen, Guangdong 518172, P. R. China
E-mail: zhangmingjian@cuhk.edu.cn

K. Nie, J. Wang

The ORCID identification number(s) for the author(s) of this article can be found under https://doi.org/10.1002/aenm.202301216

DOI: 10.1002/aenm.202301216

www.advancedsciencenews.com

www.advenergymat.de

ADVANCED ENERGY MATERIALS 16146849, 2023, 32, Downloaded from https://advanced onlinelibrary.wiely.com/doi/10.1002/aem.m.20201216 by University Town Of Shenzhen, Wiley Online Library on [2011/2025]. See the Terms and Conditions (https://onlinelibrary.wiely.com/terms-and-conditions) on Wiley Online Library for rules of use; OA archies are governed by the applicable Centwise Commons I

the role of OVs in structure regulation at the atomic level is still unclear and calls for further study.

Here, we introduce OVs at the near-surface region of a typical LROs cathode, $Li_{1,2}Ni_{0,13}Co_{0,13}Mn_{0,54}O_2$ (LR-114) through an ultra-long medium-temperature post-annealing strategy (Figure S1, Supporting Information). Different from the previous methods of generating OVs using delithiation agents,[15] the surficial OVs-rich layer is constructed by regulating the sintering strategy with Li compensation to suppress the formation of spinel. Such modification greatly increased capacity retention and lowered voltage decay in long-term cycling. Combined experimental data from in situ surface-enhanced Raman spectroscopy (SERS), operando differential electrochemical mass spectrometry (DEMS), soft X-ray absorption spectroscopy (sXAS), time-offlight secondary ion mass spectrometry (TOF-SIMS), and cryoscanning transmission electron microscopy (cryo-STEM) indicated that the surficial OVs restrained the formation of O-O dimers and O2 at the near surface, leading to the formation of a uniform and compact cathode/electrolyte interphase (CEI) layer. The CEI layer suppressed the L-S-R phase degradation in the bulk, responsible for the excellent electrochemical performance. These in-depth findings provide novel perspectives for developing LROs with high reversibility of oxygen redox.

2. Results and Discussion

2.1. Constructing Surficial OVs Layer

OVs were constructed in LR-114 by an ultra-long medium-temperature post-annealing (Figure S1, Supporting Information), and the sample was labeled as LRH-114. Scanning electron microscope (SEM) images indicate that they exhibit similar spherical secondary particles with a size of around 10 µm (Figure S2, Supporting Information), and the Mn/Co/Ni elements are uniformly distributed within individual secondary particles as illustrated in Figure S3, Supporting Information. The results of ICP-OES show that the TM ratio of LR-114 and LRH-114 are Ni:Mn:Co = 1:4:1(Table S1, Supporting Information). Rietveld refinement of X-ray diffraction (XRD) patterns (Tables S2–S4, Supporting Information) reveals that LRH-114 is composited with 98.3 wt% of layered phase (S. G. R-3m) and 1.7 wt% of spinel phase (S. G. Fd-3m) (Figure S4, Supporting Information).

To examine the distribution of OVs in LR-114 at the nanoscale, the annual dark field (ADF) imaging and electron energy loss spectra (EELS) line scan were performed by STEM. As shown in **Figure 1**a, the layered structure is well maintained in the bulk, while the outmost surface with a thickness of around 3 nm is densified (indicated by the bright contrast) and exhibits spinel-like lattice fringes. Both the surface and bulk of LR-114 maintain the layered structure (Figure S5, Supporting Information). EELS line scan was performed along the arrow in Figure 1a. As shown in Figure 1b, the pre-peak of O K-edge at around 533 eV gradually diminishes from bulk to surface, while the pre-peak of O K-edge shows no obvious intensity change from bulk to surface for LR-114 (Figure S6, Supporting Information), suggesting the formation of OVs at the surface of LRH-114.^[11] Mn L3 peak shifts to the low energy direction from bulk to surface, hinting

at the lower Mn valence at the surface, which is consistent with the formation of OVs. Quantitative analysis of element contents was carried out according to peak areas of Ni, Co, Mn, and O EELS signals. As shown in Figure 1c, O is relatively deficient at the surface region within a thickness of about 10 nm compared with that in the bulk, further confirming the enrichment of OVs at the surface. Mn distribution exhibits a similar trend with O, indicating the spatial correlation between Mn and O. In addition, Co and Ni are observed to concentrate at the outmost surface with a thickness of around 3 nm, which corresponds to the densified region observed in Figure 1a. The densified region is further depicted by the high-angle annual dark field (HAADF) image (Figure 1d), presenting a spinel-like structure, which is consistent with the XRD refinement result. It is reasonable that, surficial enrichment of OVs aggravates TM migration toward Li slabs, resulting in the phase transition from layer to spinel at the outmost surface.

Figure 1e shows O K-edge sXAS of LR-114 and LRH-114 under the surface-sensitive total electron vield (TEY) mode (with a probing depth around 4 nm). The broad feature above 535 eV is associated with transitions from O 1s to TM 4sp band mixed with O 2p states, and the two pre-edge peaks at \approx 530 and \approx 532 eV are attributed to the transitions from the O 1s to the empty TM d orbitals.^[2d] The intensity of the pre-edge peaks for LRH-114 is lower than that for LR-114, implying a reduced covalency of TM-O bond, owing to the surficial enrichment of OVs in LRH-114.^[16] Electron paramagnetic resonance (EPR) spectra of LRH-114 and LR-114 (Figure 1f) show a significant difference, and the sharp g value around 2.0015 is the characteristic response of OVs, further confirming the existence of OVs in LRH-114.^[17] In brief, the OVs layer with a thickness of about 10 nm has been successfully introduced at the surface of LRH-114, as confirmed by the STEM-EELS, sXAS, and EPR results.

2.2. Enhanced Reversibility of Lattice O Redox

To investigate the influence of OVs on the surface chemical/structural changes, in situ SERS was performed on LR-114 (Figure 2a) and LRH-114 (Figure 2b) during the initial cycle. Figure S7, Supporting Information, presents the design details of the in situ SERS battery. The peaks at about 600 and 480 cm $^{-1}$ are related to TM-O stretching vibration (A_{1g}) and O-TM-O bending vibration (E_o) in the layered phase (S.G. R-3m), respectively. As for LR-114, the two peaks disappear when charged above 4.5 V and then re-appear at the end of discharge, but the peak intensities become weaker, indicating poor structural reversibility. As for LRH-114, the two peaks are highly symmetric with charge/discharge, presenting strong structural reversibility. The in situ XRD in the first cycle shows a similar trend (Figure S8, Supporting Information). Moreover, the signal of oxidized peroxides $((O_2)^{n-}, 850 \text{ cm}^{-1})$ appears as early as 4.45 V in the charge process of LR-114, and keeps aggressive in the whole high-voltage period, indicating a serious O-O dimerization process, which would lead to severe lattice O loss. Correspondingly, the electrolyte oxidization species were also noticed at about 950, 1050, and 1200 cm⁻¹, which can be ascribed to the violent parasitic reactions between the (O2)n- species and the electrolyte.[18] In contrast, the signal of oxidized peroxides in LRH-114 appears

16146840, 2023, 32, Downloaded from https://advanced.onlinelibrary.wiely.com/doi/10.1002/wenn.202301216 by University Town Of Shenzhen, Wiley Online Library on [20/11/2025]. See the Terms and Condition (https://onlinelibrary.wiely.com/terms

and-conditions) on Wiley Online Library for rules of use; OA articles are governed by the applicable Creative Commons

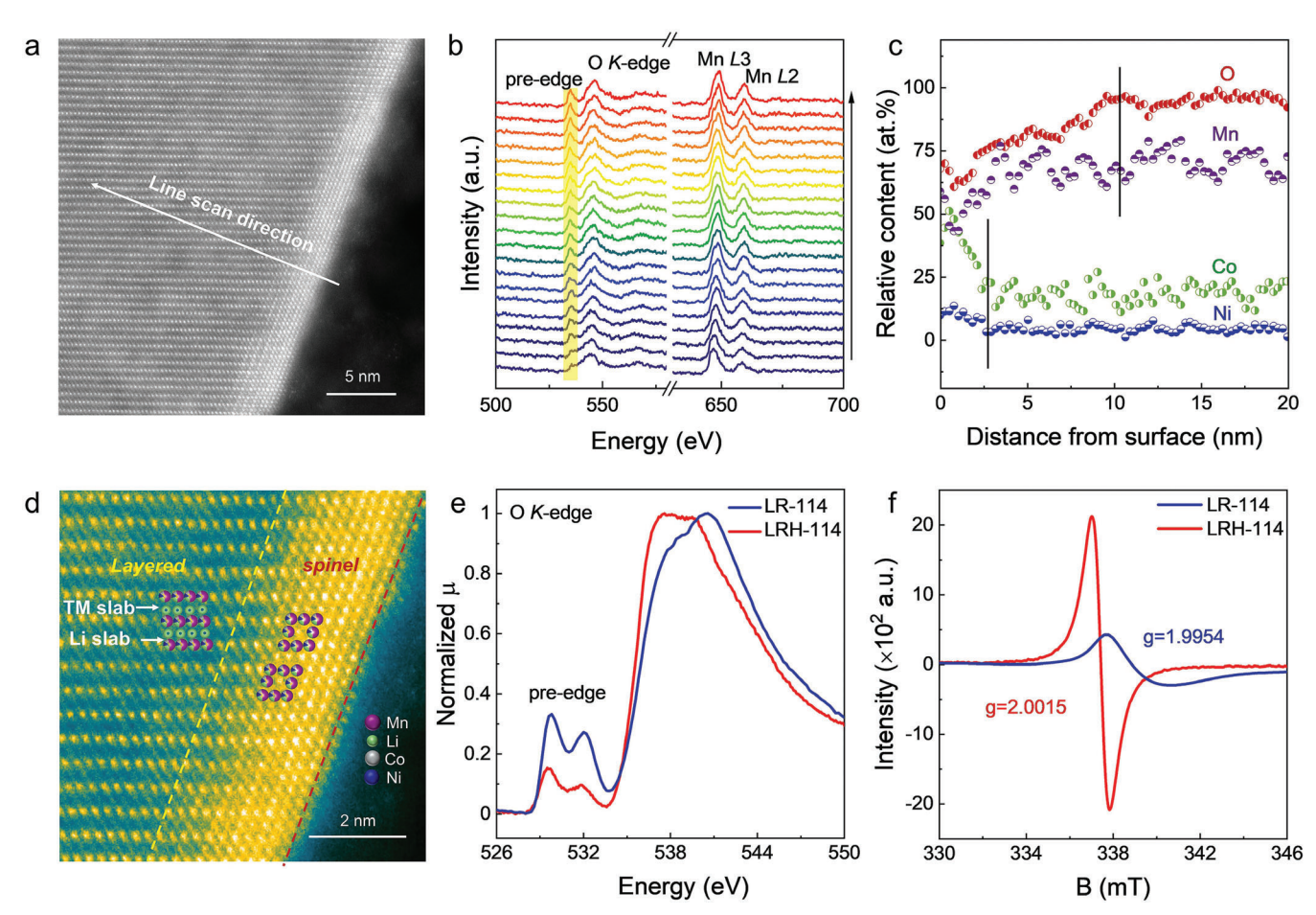


Figure 1. Formation of surficial OVs in LRO cathode. a) ADF-STEM image of LRH-114. b) STEM-EELS spectra of LRH-114 recorded along the arrow marked in (a), pointing from the surface to the bulk. c) Relative contents of O (red), Mn (violet), Co (green), and Ni (blue) as a function of the position, derived by the integrated intensity of the corresponding EELS peaks in (b). d) HADDF-STEM image of the surface region of LRH-114 from (a). The region between the red dotted line and the yellow dotted line is the densification layer. e) O K-edge sXAS spectra of LR-114 and LRH-114 under the TEY mode. f) EPR spectra of LR-114 and LRH-114 at room temperature in Ar.

at a higher voltage, and the corresponding content is greatly decreased. Mutually verified, the electrolyte decomposition signals are also reduced. These results demonstrate that OVs enrichment at the surface can effectively suppress the formation of O-O dimers, and reduce the surficial side reactions, which should be conducive to structural reversibility.

Operando DEMS experiments were performed to evaluate the gas evolution during the charge process, which is a very sensitive way to study oxygen behaviors. [19] During the charge process in LR-114 (Figure 2c), massive O_2 is produced at a low onset voltage of about 4.45 V and then followed by the CO_2 evolution at 4.55 V from the electrolyte decomposition. [20] Differently, for LRH-114 (Figure 2d), the gas production onsets of O_2 and CO_2 are 4.55 and 4.6 V, respectively, which are higher than that in LR-114 material. Moreover, CO_2 and O_2 release contents by LRH-114 are about 1/10 and 1/20 of that in LR-114 based on the integral areas. The DEMS results suggest that the irreversible lattice oxygen loss is significantly delayed and reduced in LRH-114. These results are consistent with the Raman spectra, confirming that the surficial OVs can hinder O-O dimerization and thus greatly suppress the evolution of O_2 and CO_2 gases.

2.3. Improved Electrochemical Performance

The electrochemical performance was evaluated to investigate the effect of the introduced OVs. The first charge/discharge profiles of LRH-114 and LR-114 in Figure 3a show similar discharge capacities of around 300 mA h g^{-1} at 0.1 C (1 C = 250 mA g-1). Notably, the small discharge plateau at around 2.6 V for LRH-114 is related to the spinel phase, [21] which is confirmed by the corresponding dQ/dV curve (Figure 3b). LRH-114 exhibits better rate performance (Figure S9, Supporting Information), and the larger Li⁺ diffusion coefficients (D_{Li}^+) derived from the GITT data (Figure S10, Supporting Information). Galvanostatic electrochemical impedance spectra (GEIS) (Figure S11, Supporting Information) and relaxation time distribution (DRT) technology (Figure S12, Supporting Information) show that LRH-114 has a smaller charge transfer impedance in the CEI during the first charge and discharge process. Then, the cycling stability is compared at 0.5 C in half cells (Figure 3c,d). LRH-114 demonstrates a smaller voltage decay after 200 cycles (1.5 mV per cycle) compared to LR-114 (2.4 mV per cycle) (Figure 3c), confirmed by the corresponding dQ/dV curves (Figure S13, Supporting

16146480, 2023, 32, Dwnholaded from https://advanced.onlinelibrary.wiely.com/doi/10.1002/aena.m.20201216 by University Town Of Sheraben, Wiley Online Library on [2011.1025], See he Terms and Conditions (https://onlinelibrary.wiely.com/terms-and-conditions) on Wiley Online Library for rules of use; OA articles are governed by the applicable Cerative Commons

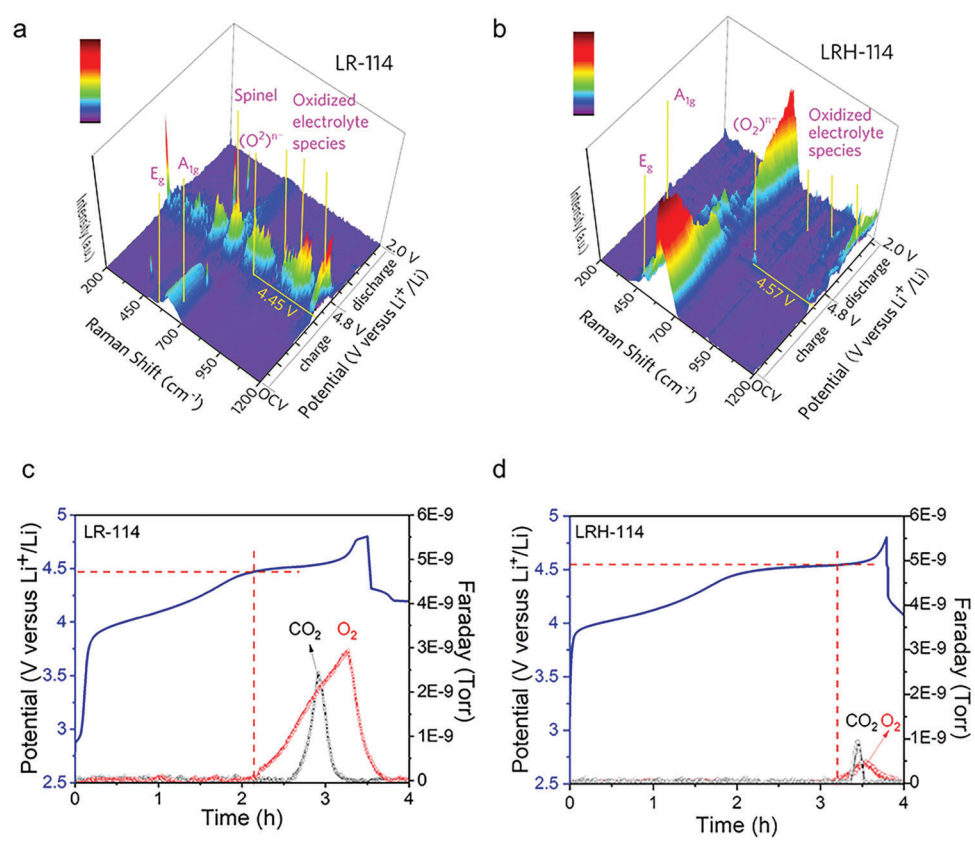


Figure 2. The lattice O redox during the first cycle of LR-114 and LRH-114. a,b) In situ SERS during the first charge/discharge of LR-114 (a) and LRH-114 (b). The Raman peaks are well assigned in the plots. c,d) Operando DEMS results, as well as the corresponding charge—discharge curves, of LR-114 (c) and LRH-114 (d).

Information) and CV profiles (Figure S14, Supporting Information). The corresponding capacity retention of LRH-114 after 200 cycles is 86.6%, superior to that of LR-114 (57.2%) (Figure 3d). Additionally, the impedance values were confined to a low level in LRH-114 even after 200 cycles (Figure S15, Supporting Information). Full cells were also assembled with pre-lithiated SiO_x anodes to further validate the cycling stability. After 200 cycles at 2 C, LRH-114 delivers a larger capacity retention of 86.9% than LR-114 (74.9%, Figure 3e). In short, the introduction of surface OVs effectively suppresses voltage decay and improves cycling stability.

2.4. Impact on Bulk Structural Stability

High-resolution transmission electron microscopy (HRTEM) and Raman spectra were employed to characterize the structural changes during cycling. Pristine LR-114 (**Figure 4**a) has an intact surface with Li₂MnO₃-type (S. G. *C2/m*) layered phase, which is identified by the superlattice fringes in the corresponding fast Fourier transform (FFT) map. The surface of LRH-114 (Figure 4b) is mostly the layered phase with a 2–3 nm-thick spinel layer (identified by the corresponding FFT map). Both exhibit the (003) lattice plane with the same interplanar space of 4.78 Å, hinting at the same bulk structure. After 100 cycles, the near-surface region of LR-114 (marked by the dotted ellipse in

Figure 4c) almost transforms into a spinel structure hybridized with partial rock-salt feature (identified by the corresponding FFT map), while LRH-114 still preserves the layered phase in the bulk with partial spinel phase at the outmost surface (identified by the corresponding FFT maps in Figure 4d). After 200 cycles (Figure 4e), more atomic disordering and severe lattice distortion appear in LR-114, evidenced by the dispersion of the reflections in the FFT map. The surface area is completely transformed into the spinel phase and rock-salt phase. [7] In sharp contrast, LRH-114 still maintains a layered phase mostly in the bulk area although a \approx 10 nm-thick surface region completely transforms to a rock-salt phase (Figure 4f). The results embody the superior capability of the OVs-rich surface in protecting the bulk lattice structure.

Ex situ Raman spectroscopy was applied to further probe the evolution of the phase composition at the surface region since it has the unique capability to figure out the short-range local structure of oxygen, that is, the O-TM coordination configuration. As shown in Figure 4g, the $E_{\rm g}$ and $A_{\rm 1g}$ peaks at about 480 and 600 cm⁻¹ come from the typical layered structure (S. G. R-3m). The weak peak at about 420 cm⁻¹ is attributed to the phonon vibration of the Li₂MnO₃-type layered phase (S. G. C2/m). A pronounced shoulder peak at about 650 cm⁻¹ can be attributed to the Mn—O stretching vibrations in the spinel phase (S. G. Fd-3m). It is clear that the content of the layer phase decreases and a large number of spinel phases is generated after 100 cycles. After

16146840, 2023, 32, Downloaded from https://advancec

onlinelibrary.wiley.com/doi/10.1002/aemm.202301216 by University Town Of Shenzhen, Wiley Online Library on [20/11/2025]. See the Terms

and-conditions) on Wiley Online Library for rules of use; OA articles are governed by the applicable Creative Commons

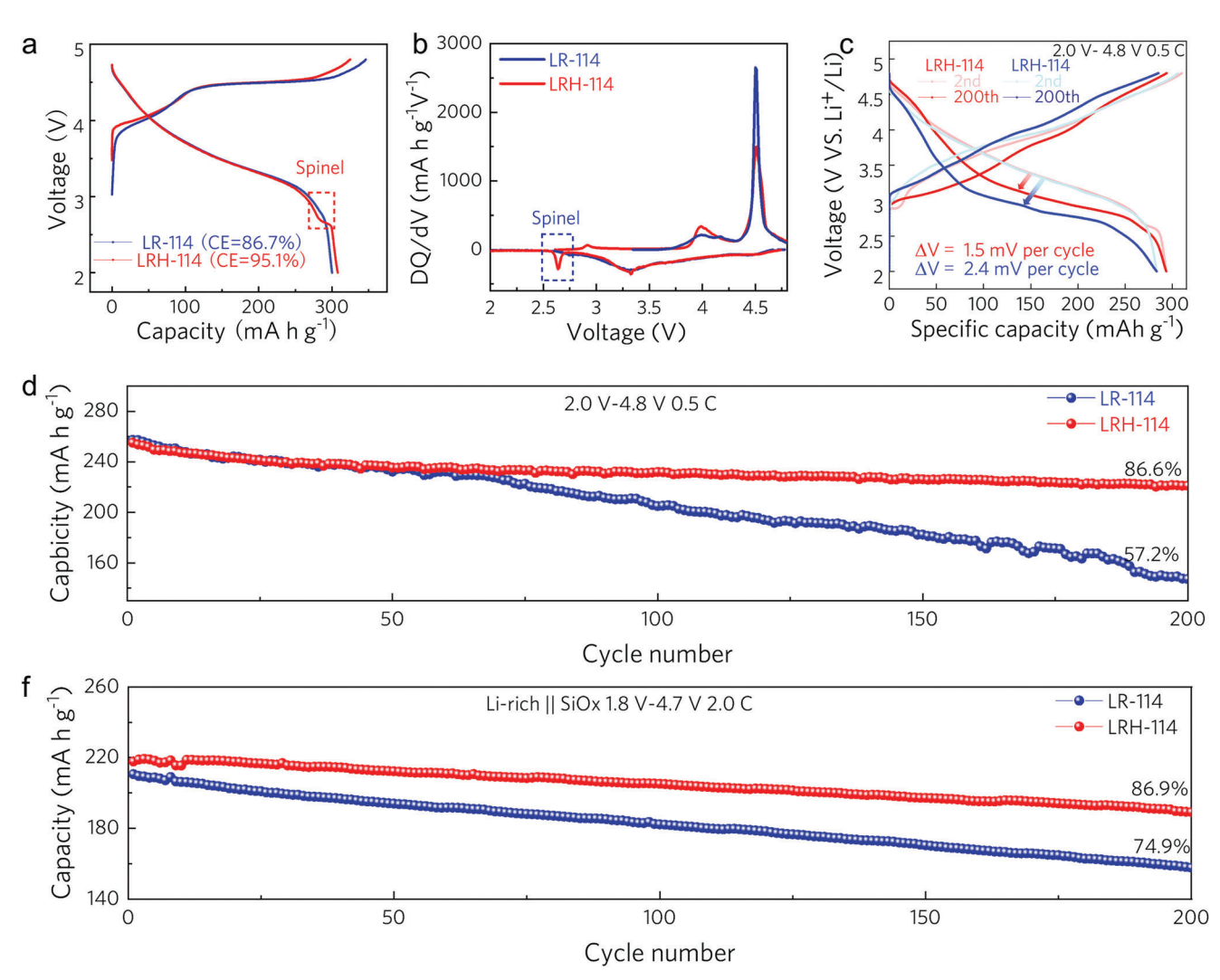


Figure 3. Electrochemical performance of LR-114 and LRH-114 cathodes. a) Charge–discharge curves of the initial cycle at 0.1 C (1 C = 250 mA g^{-1}). b) The corresponding dQ/dV curves of the initial cycle. c) Normalized discharge curves of LR-114 and LRH-114 at the 2nd and 200th cycles. d) Cycling performance of LR-114 and LRH-114 coin half cells within 2–4.8 V at 0.5 C. e) Cycling performance of LR-114 and LRH-114 full cells coupled with SiO_x anodes within 1.8–4.7 V at 2 C.

200 cycles, LR-114 turns completely disordered as Raman peaks fade away, which is consistent with the HRTEM results. As to LRH-114 (Figure 4h), it contains a majority of layered phases and a certain amount of spinel phase at the surface before cycling. After 100 cycles, the composition changes little, indicated by the indistinct profile change. After 200 cycles, Li₂MnO₃-type layered phase disappears, and the content of the spinel phase increases, while the layered phase is still dominant. It is consistent with the XRD results of long-cycled electrodes (Figure S16, Supporting Information).

O K-edge sXAS (TEY mode) were recorded on LR-114 (Figure 4i) and LRH-114 (Figure 4j) electrodes after 100 and 200 cycles. The peak intensity of LR-114 at \approx 532 eV is apparently reduced after 200 cycles, which can be attributed to the serious lattice O loss at the surface. Whereas the peak of LRH-114 keeps nearly unchanged from the 100th to 200th cycle, indicating that the lattice O loss is effectively suppressed. Mn L-edge sXAS (TEY mode) of LR-114 (Figure 4k) and LRH-114 (Figure 4l)

were also measured to check the valence change of surficial Mn element. It is clear that LR-114 and LRH-114 mainly have Mn⁴⁺ at the surface before cycling. After 100 cycles, most of the Mn⁴⁺ at the surface is reduced to Mn³⁺/Mn²⁺ for both LR-114 and LRH-114. After 200 cycles, Mn⁴⁺ at the surface of LR-114 completely disappears while there is still part of Mn⁴⁺ at the surface of LRH-114. Similarly, Co and Ni are also greatly reduced after 100 and 200 cycles (Figure S17, Supporting Information). These TM reductions correspond to the surface structural degradation observed by HRTEM. Moreover, in situ UV–vis absorption spectroscopy shows that LRH-114 has less TM dissolution during the first charge (Figure S18, Supporting Information), which hints at the formation of less Mn³⁺ and the suppressed TM migration.^[25]

The combined results of HRTEM and Raman demonstrate the better structure stability of LRH-114 after long cycles, and the sXAS results demonstrate less O loss and TM migration in LRH-114 during cycling. They can

16146840, 2023, 32, Downloaded from https://advancec

onlinelibrary.wiley.com/doi/10.1002/aenm.202301216 by University Town Of Shenzhen, Wiley Online Library on [20/11/2025]. See the Terms and Conditions (https://onlinelibrary.wiley.com/term

ınd-conditions) on Wiley Online Library for rules of use; OA articles are governed by the applicable Creative Common

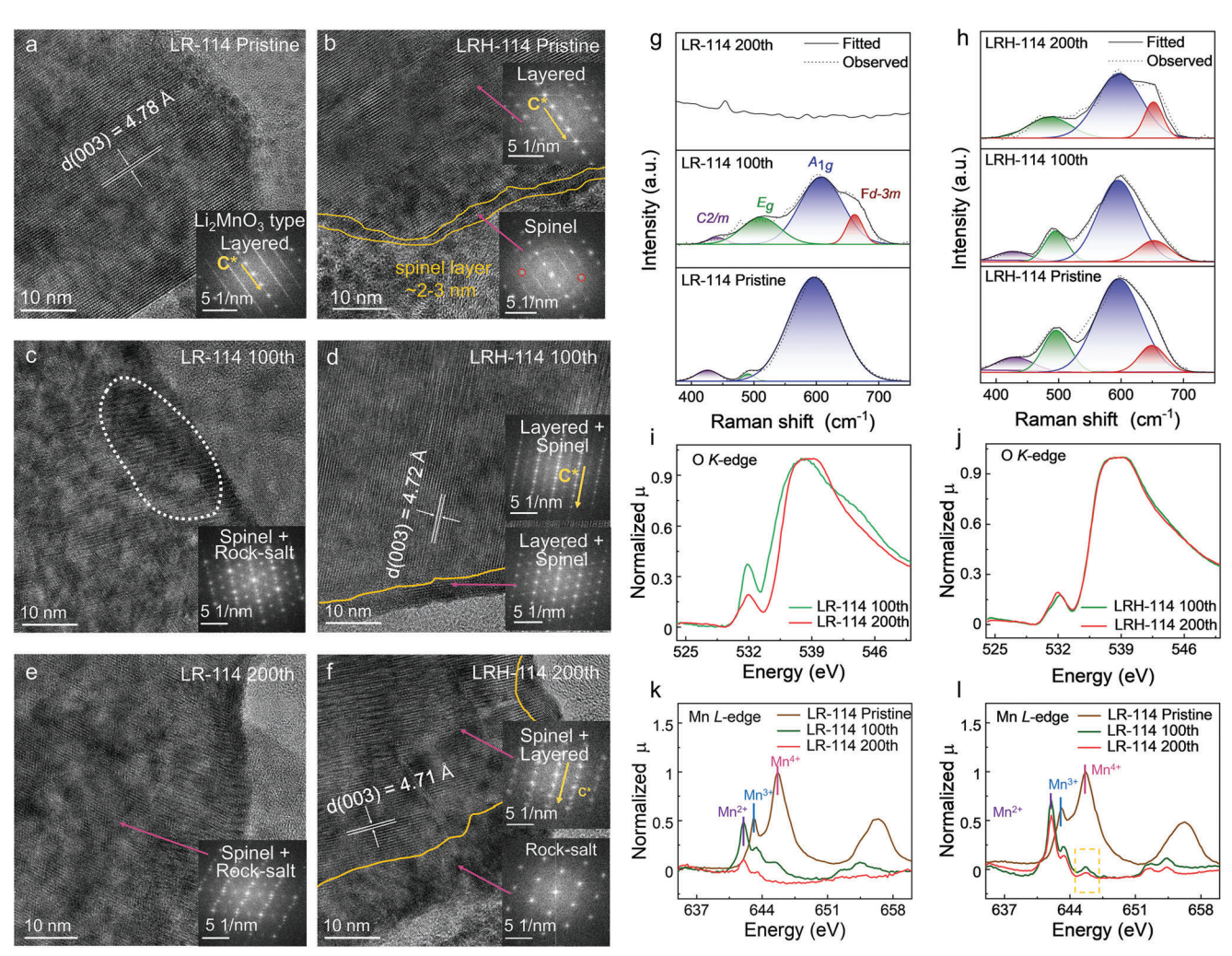


Figure 4. Structure stability of LR-114 and LRH-114 with cycling. HRTEM images of pristine LR-114 (a), LR-114 after 100 cycles (b), LR-114 after 200 cycles (c), pristine LR-114 (d), LR-114 after 100 cycles (e), and LRH-114 after 200 cycles (f). Insets: the FFT maps of corresponding areas. Raman spectra of LR-114 (g) and LRH-114 (h) before cycling, after 100 and 200 cycles. O K-edge sXAS spectra of LR-114 (i) and LRH-114 (j) after 100 and 200 cycles at 1 C under the TEY mode. Mn L-edge sXAS spectra of LR-114 (k) and LRH-114 (l) before cycling and after 100 and 200 cycles at 1 C under the TEY mode.

be ascribed to the protection role of the OVs-rich surface, and responsible for the improved electrochemical performance.

2.5. Impact on CEI

TOF-SIMS with high surface sensitivity and chemical selectivity was employed to explore the impact of OVs-rich surface on the chemical evolution of the CEI layers (**Figure 5**a,–d and Figures S19–S25, Supporting Information). As shown in Figure 5a–d, the $\operatorname{LiF_2}^-$ signal of LR-114 is stronger than that of LRH-114 after 10 cycles, hinting at the earlier formation and fast accumulation of LiF on the surface of LR-114, which may be related to the serious side reactions in the initial cycles. After 50 cycles, the LiF distribution in LR-114 becomes more inhomogeneous. As to LRH-114, it presents a uniform distribution of LiF species among the first 50 cycles, and the corresponding intensity is weaker than

that of LR-114. The uniform LiF species on the surface of LRH-114 with the appropriate content provide better protection for the electrolyte against further oxidation.^[25] The MnF₃⁻ signal becomes more intense with cycling for LR-114, which suggests continuous TM dissolution. [26] In contrast, the MnF₃- signal for LRH-114 remains weak even after 50 cycles, indicating the suppressed TM dissolution, which is further confirmed by the NiF₃ distribution (Figure S19, Supporting Information). The thickness of the CEI layer can be roughly compared by the MnO₂- signal (Figure 5a-d) and the MnO- signal (Figure S20, Supporting Information). It is clear that LRH-114 has a thinner and more uniform CEI layer after long cycles. The C2HO- signals are decreased in LRH-114 compared with that in LR-114 after 10 and 50 cycles, suggesting the suppression of organic solvent decomposition, which can be ascribed to the reduced highly oxidizing species, that is, O-O dimers (O2n-).[26] PO2- and POF2- fragments come from the decomposition of LiPF6 associated with released oxygen. [26] PO2- and POF2- (Figure S21, Supporting

16146849, 2023, 32, Dwnholaded from https://advanced.onlinelibrary.wiely.com/oi/0101002/aem.20.20201216 by University Town Of Shenzhen, Wiley Online Library on [20111025]. See the Terms and Conditions (https://onlinelibrary.wiely.com/terms-and-conditions) on Wiley Online Library for rules of use; OA articles are governed by the applicable Creative Commons

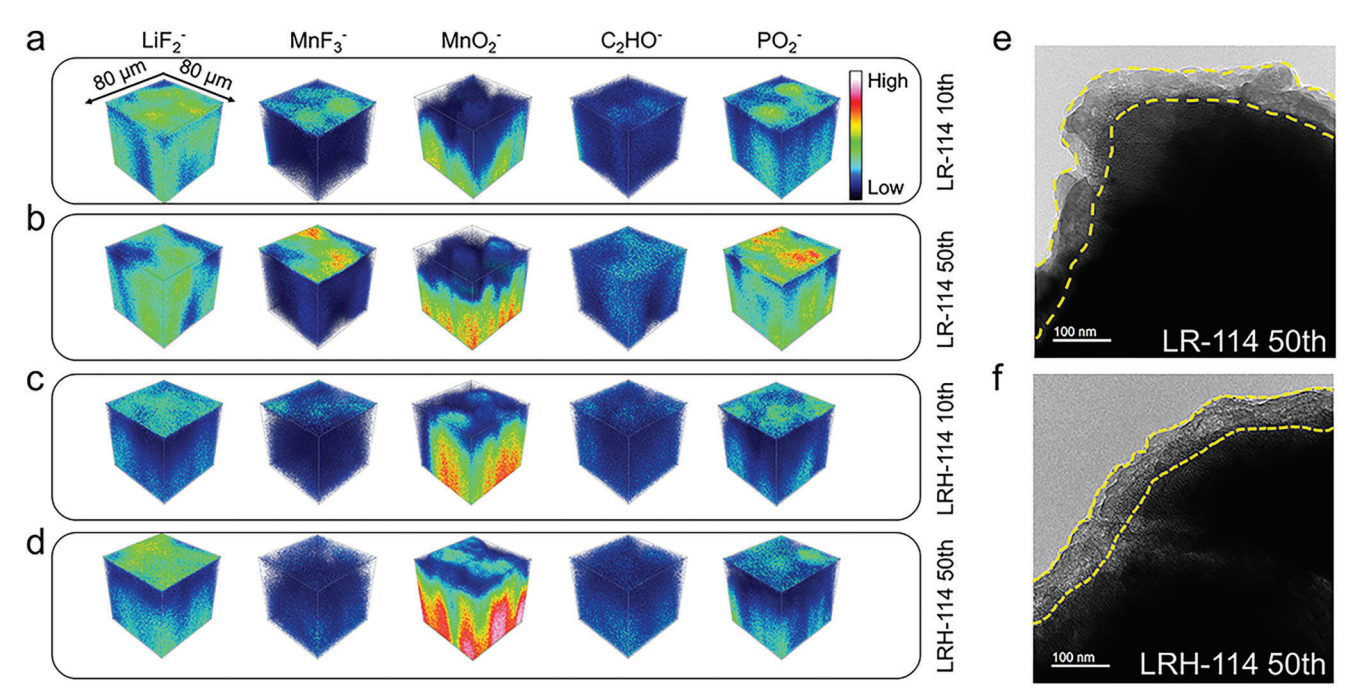


Figure 5. 3D distribution for LiF_2^- , MnF_3^- , MnO_2^- , C_2HO^- , and PO_2^- signals for LR-114 cathodes after 10 cycles (a), 50 cycles (b), and for LRH-114 cathodes after 10 cycles (c), 50 cycles (d), derived by the corresponding TOF-SIMS results. Cryo-STEM images for LR-114 (e) and LRH-114 (f) after 50 cycles.

Information) have the same trend as C_2HO^- , further verifying the suppressed side reactions. In brief, benefiting from the OVsrich surface, a thinner and more uniform CEI layer with LiF as the main component was formed on the surface of LRH-114.

The morphology of CEI layers after 50 cycles was further examined by cryo-STEM.^[27] As shown in Figure 5e,f, LRH-114 has a more compact and uniform CEI layer than LRH-114, consistent with TOF-SIMS results. Such a CEI layer can favor efficient Li⁺ transport and suppress diverse side reactions at the interface thus protecting the interior structure of LROs.^[26]

2.6. Mechanism Understanding

Combining all the results above together, the mechanism of the improved electrochemistry by surficial enrichment of OVs is illustrated in Figure 6. The OVs enriched at the surface of LRH-114 greatly suppress the formation of O-O dimers O_2^{n-} (0 < n < 4) by decreasing the possibility of O-O dimerization. Then all the relevant side reactions initiated by the highly-oxidizing O₂ndimers, including the decomposition of organic solvents (EC, DMC, etc.) and the hydrolysis of the solute LiPF₆, would be significantly suppressed. Correspondingly, the by-products, including CO₂, H₂O, HF, and LiF, are also decreased. [28] By slowing down the kinetics of these side reactions, a thin and compact CEI layer is constructed uniformly on the surface. Since LiF is the main component of the CEI layer, the enhanced robustness enables CEI to resist the corrosion of HF and mitigate TM dissolution efficiently.[29] Finally, the bulk structure can be well protected and the L-S-R structural degradation was greatly mitigated even after

prolonged cycling, [30] which explains the improved electrochemical performance.

3. Conclusion

In summary, a surficial OVs layer was successfully introduced into the LROs by a long-time medium-temperature postannealing strategy, which greatly improved the cycling stability, validated in both half and full cells. The role of surficial OVs was thoroughly investigated by combining various advanced characterization techniques including in situ SERS, operando DEMS, sXAS, TOF-SIMS, and cryo-STEM. It reveals that surficial OVs can greatly reduce the dimerization of lattice O, which thus suppresses the side reactions initiated by O-O dimers and helps to construct a uniform and compact CEI layer on the surface of LROs. The CEI layer can effectively protect the bulk structure from harmful TM dissolution and structural degradation in LROs, eventually delivering higher cycling stability and less voltage decay. These in-depth understandings of OVs would benefit the design of new high-performance cathode materials based on anionic redox chemistry.

4. Experimental Section

Electrochemical Testing: All the electrochemical measurements were conducted using CR2032-type coin cells. Active material, conductive acetylene black (AB), and polyvinylidene difluoride (PVDF) binder with a weight ratio of 8:1:1 were mixed and evenly cast onto Al foil and punched into the discs with a diameter of 10 mm after drying. The coin cells were assembled with the discs as the cathode, Li foils as the anode, Celgard films as the separator, and 1 m LiPF₆ solution in EC/DMC (EC: ethylene carbonate, DMC: dimethyl carbonate, weight ratio of 1:1) as the elec-

16146840, 2023, 32, Downloaded from https://advanced.onlinelibrary.wiley.com/doi/10.1002/aemm.202301216 by University Town Of Shenzhen, Wiley Online Library on [2011/2025]. See the Terms and Conditions (https://onlinelibrary.wiley.com/terms

and-conditions) on Wiley Online Library for rules of use; OA articles are governed by the applicable Creative Common

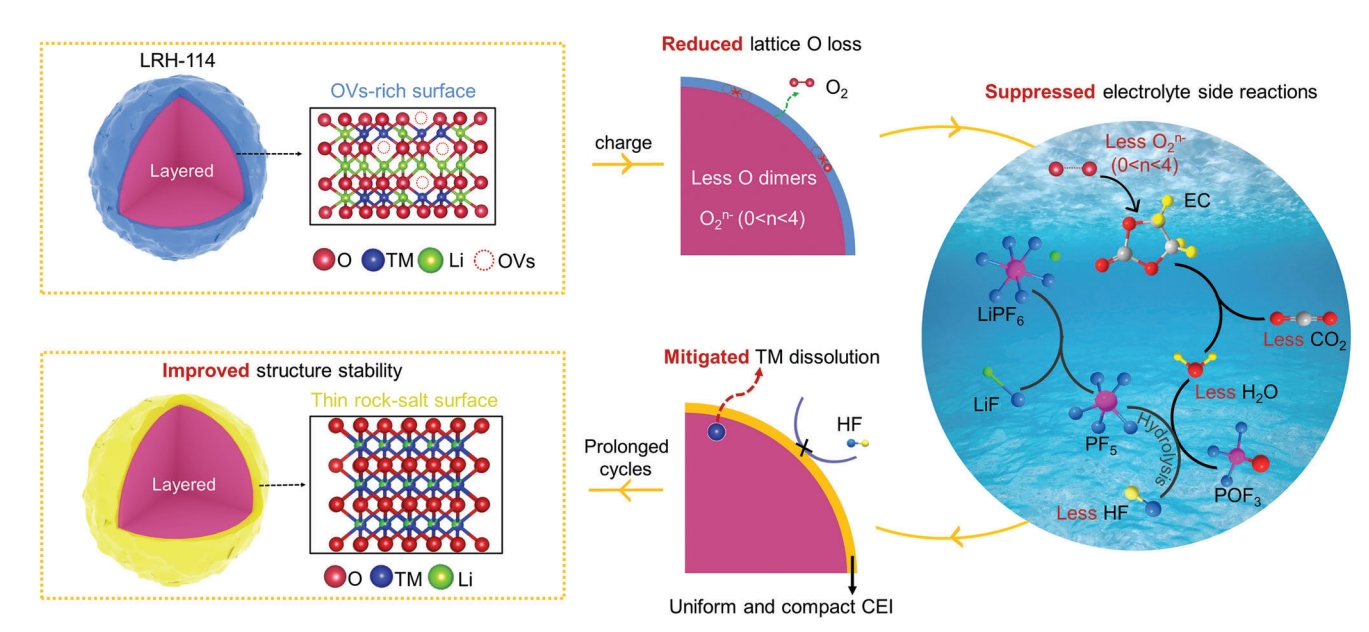


Figure 6. Schematic illustration of the role of OVs-rich surface in stabilizing the interface and protecting the interior structure of LROs.

trolyte in an Ar-filled glovebox (Mikrouna, China). The assembled cells were tested with the NEWARE battery test system at room temperature. The cyclic voltammetry (CV) and electrochemical impedance spectroscopy (EIS) tests were performed by the electrochemical workstation (Solartron, America). To assemble the full cells, commercial SiO_x , AB, and carboxymethyl cellulose (CMC) binder with a weight ratio of 8:1:1 were blended and cast onto Cu foil and then punched into the discs with a diameter of 12 mm as the anode. The SiO_x anode was pre-lithiated by directly touching with Li foil and the electrolyte for 10 h in an Ar-filled glovebox. $^{[31]}$

Characterizations: The powder XRD patterns were obtained from Bruker D8 Advance X-ray diffractometer. The morphology and elemental distribution were measured by SEM (Carl Zeiss SUPPA@ 55), equipped with an energy-dispersive X-ray spectrometer (EDS). The TEM images and EELS were collected by HRTEM (JEOL JEM-3200FS) and HADDF-STEM (FEI Titan Themis G2). The sXAS measurements were carried out in the TEY mode under ultra-high vacuum at beamline 4B9B of Beijing Synchrotron Radiation Facility of the Institute of High Energy Physics, Chinese Academy of Sciences. Au 4f7/2 core level spectra were recorded for the photon energy calibration, and the energy resolution was better than 0.2 eV at room temperature. EPR measurement was conducted by a Bruker EMX-PLUS 10/12 instrument with a microwave frequency of \approx 9.8 GHz (X band) and a microwave power of 2 mW. The center field was 3500 G and the swept width was 100 G. The field was modulated at a frequency of 100 kHz at 1 G amplitude. [15,32] In the cryo-STEM test, the battery was disassembled in an argon-filled glove box and washed with DMC to remove the lithium salts. After disassembling the battery, carefully dripped \approx 50 μ L onto the TEM grid. Immediately after rinsing, sealed the sample in an airtight container, submerged it in liquid nitrogen, and crushed the container to quickly expose the sample to refrigerant without any air exposure. When immersed in liquid nitrogen, the sample was loaded into a STEM holder (Gatan 626) and inserted into the TEM column. The cryo-STEM holder used a dedicated shutter to prevent air exposure and condensation onto the sample, thus keeping the sample in its native state. Once inside the TEM column, the temperature was always maintained at approximately -178 °C. [27b] TOF-SIMS analysis was performed using the TOF-SIMS spectrometer (TESCAN GAIA3). All detected secondary ions were in a mass range of 0-900 aum and possessed negative polarity. The pulsed 30 keV Bi₁⁺ ion beam in a high current mode was used for depth profiling and 1000 eV Cs⁺ was used as the sputtering ion beam in a typical sputtered area (80 \times 80 $\mu m).^{[25a]}$

The ECC-DEMS cell (EL-CELL, Germany) and on-line electrochemical mass spectrometry (HPR-20 EGA) were utilized for the operando DEMS test. The evolved gases were detected in the mass spectrometer along with the galvanostatic charging process performed by a NEWARE battery tester.

All Raman spectra were recorded by Renishaw inVia with the 633 nm laser light source. To obtain an enhanced Raman signal, the $Au@SiO_2$ nanoparticle dispersed solution (PERSER-TECH, CP-2, Xiamen) was dropped onto the cathode and dried at 110 °C in a vacuum. For in situ Raman measurement, a CR2032-type coin cell was assembled. A small hole (1.5 cm \times 1.5 cm) was punched on the top of the cell in advance and covered by a thin sapphire window (200 µm-thick, 2 cm-diameter) for the laser and Raman signals entry and collection. The laser beam power delivered to the electrode surface was 10% of the maximum 17 mW intensity. The Raman spectrum acquisition time was about 300 s with a 100 s pause. During the in situ test, the potential was scanned from OCV to 4.8 V, and then to 2 V at the rate of 0.1 mV s $^{-1}$ on an electrochemical workstation (Solartron, America).

The in situ UV–vis spectra were collected from a quartz cuvette assembled with the cathode, Li foil, and 1.5 mL electrolyte by a UV–vis spectrometer (UV2600, Shimadzu). The potential was driven by CV measurement at the rate of 0.2 mV s $^{-1}$ in the Solartron electrochemical workstation.

Supporting Information

Supporting Information is available from the Wiley Online Library or from the author.

Acknowledgements

K.W. and J.Q. contributed equally to this work. This work was financially supported by the National Natural Science Foundation of China (52172175, 52202269), the Shenzhen Science and Technology Research Grant (JCYJ20210324130812033, JCYJ20200109140416788, GXWD20201231165807007-20200807111854001), Soft Science Research Project of Guangdong Province (No. 2017B030301013), the Program from Guangdong Introducing Innovative and Entrepreneurial Teams (2019ZT08L101 and RCTDPT-2020-001), the Shenzhen Key Laboratory of Eco-materials and Renewable Energy (ZDSYS20200922160400001), the

ADVANCED ENERGY MATERIALS

16146840, 2023, 32, Downloaded from https://advanced.onlinelibrary.wiley.com/doi/10.1002/aemn.202301216 by University Town Of Shenzhen, Wiley Online Library on [2011/2025]. See the Terms and Conditions (https://onlinelibrary.wiley.com/terms/

and-conditions) on Wiley Online Library for rules of use; OA articles are governed by the applicable Creative Common

Basic and Applied Basic Research Foundation of Guangdong Province (No. 2021B1515130002), the National Key R&D Program of China (2020YFB0704500), and the Major Science and Technology Infrastructure Project of Material Genome Big-science Facilities Platform supported by Municipal Development and Reform Commission of Shenzhen. Eceshi is thanked for the TOF-SIMS test. A spelling mistake affecting the appearance of M.J. in the author byline was rectified after initial online publication, on August 25, 2023.

Conflict of Interest

The authors declare no conflict of interest.

Data Availability Statement

The data that support the findings of this study are available in the supplementary material of this article.

Keywords

cathode/electrolyte interphase, cycling stability, Li-rich layered oxides, O-O dimers, oxygen vacancies

Received: April 24, 2023 Revised: June 30, 2023 Published online: July 11, 2023

- a) G. Crabtree, Science 2019, 366, 422; b) M. F. Toney, Nat. Energy 2019, 4, 1014; c) M. Li, J. Lu, Z. Chen, K. Amine, Adv. Mater. 2018, 30, 1800561; d) P. Guan, L. Zhou, Z. Yu, Y. Sun, Y. Liu, F. Wu, Y. Jiang, D. Chu, J. Energy Chem. 2020, 43, 220.
- [2] a) J. Lee, D. A. Kitchaev, D.-H. Kwon, C.-W. Lee, J. K. Papp, Y.-S. Liu, Z. Lun, R. J. Clement, T. Shi, B. D. McCloskey, J. Guo, M. Balasubramanian, G. Ceder, Nature 2018, 556, 185; b) J. Xu, M. Sun, R. Qiao, S. E. Renfrew, L. Ma, T. Wu, S. Hwang, D. Nordlund, D. Su, K. Amine, J. Lu, B. D. McCloskey, W. Yang, W. Tong, Nat. Commun. 2018, 9, 947; c) W. S. Yoon, M. Balasubramanian, K. Y. Chung, X. Q. Yang, J. McBreen, C. P. Grey, D. A. Fischer, J. Am. Chem. Soc. 2005, 127, 17479; d) K. Luo, M. R. Roberts, R. Hao, N. Guerrini, D. M. Pickup, Y. S. Liu, K. Edstrom, J. H. Guo, A. V. Chadwick, L. C. Duda, P. G. Bruce, Nat. Chem. 2016, 8, 684; e) A. Grimaud, W. T. Hong, Y. Shao-Horn, J. M. Tarascon, Nat. Mater. 2016, 15, 121; f) A. J. Perez, Q. Jacquet, D. Batuk, A. Iadecola, M. Saubanere, G. Rousse, D. Larcher, H. Vezin, M.-L. Doublet, J.-M. Tarascon, Nat. Energy 2017, 2, 954; g) X. Li, Y. Qiao, S. Guo, Z. Xu, H. Zhu, X. Zhang, Y. Yuan, P. He, M. Ishida, H. Zhou, Adv. Mater. 2018, 30, 1807825.
- [3] a) V. N. Hung, J. C. Im, S. Unithrattil, W. B. Im, J. Mater. Chem. A 2018, 6, 19445; b) M. Li, T. Liu, X. Bi, Z. Chen, K. Amine, C. Zhong, J. Lu, Chem. Soc. Rev. 2020, 49, 1688; c) A. J. Naylor, E. Makkos, J. Maibach, N. Guerrini, A. Sobkowiak, E. Bjoerklund, J. G. Lozano, A. S. Menon, R. Younesi, M. R. Roberts, K. Edstroem, M. S. Islam, P. G. Bruce, J. Mater. Chem. A 2019, 7, 25355.
- [4] a) M. Sathiya, A. M. Abakumov, D. Foix, G. Rousse, K. Ramesha, M. Saubanere, M. L. Doublet, H. Vezin, C. P. Laisa, A. S. Prakash, D. Gonbeau, G. VanTendeloo, J. M. Tarascon, *Nat. Mater.* 2015, 14, 230; b) E. McCalla, A. M. Abakumov, M. Saubanere, D. Foix, E. J. Berg, G. Rousse, M.-L. Doublet, D. Gonbeau, P. Novak, G. Van Tendeloo, R. Dominko, J.-M. Tarascon, *Science* 2015, 350, 1516.
- [5] a) B. Song, Z. Liu, M. O. Lai, L. Lu, Phys. Chem. Chem. Phys. 2012, 14, 12875; b) M. Gu, I. Belharouak, J. Zheng, H. Wu, J. Xiao, A. Genc,

- K. Amine, S. Thevuthasan, D. R. Baer, J.-G. Zhang, N. D. Browning, J. Liu, C. Wang, ACS Nano 2013, 7, 760; c) A. Boulineau, L. Simonin, J.-F. Colin, E. Canevet, L. Daniel, S. Patoux, Chem. Mater. 2012, 24, 3558; d) D. Luo, S. Fang, Q. Tian, L. Qu, L. Yang, S.-i. Hirano, Nano Energy 2016, 21, 198; e) D. Luo, G. Li, C. Fu, J. Zheng, J. Fan, Q. Li, L. Li, Adv. Energy Mater. 2014, 4, 1400062; f) D. Luo, S. Fang, L. Yang, S.-i. Hirano, J. Mater. Chem. A 2016, 4, 5184.
- [6] C. R. Fell, D. Qian, K. J. Carroll, M. Chi, J. L. Jones, Y. S. Meng, Chem. Mater. 2013, 25, 1621.
- [7] D. Qian, B. Xu, M. Chi, Y. S. Meng, Phys. Chem. Chem. Phys. 2014, 16, 14665.
- [8] H. C. Shim, D. Kim, D. Shin, S. Hyun, C.-S. Woo, T. Yu, J.-P. Ahn, Phys. Chem. Chem. Phys. 2017, 19, 1268.
- [9] Y. Okamoto, J. Electrochem. Soc. 2012, 159, A152.
- [10] P. Yan, J. Zheng, Z.-K. Tang, A. Devaraj, G. Chen, K. Amine, J.-G. Zhang, L.-M. Liu, C. Wang, Nat. Nanotechnol. 2019, 14, 602.
- [11] B. Qiu, M. Zhang, L. Wu, J. Wang, Y. Xia, D. Qian, H. Liu, S. Hy, Y. Chen, K. An, Y. Zhu, Z. Liu, Y. S. Meng, Nat. Commun. 2016, 7, 12108.
- [12] Q. Ma, Z. Chen, S. Zhong, J. Meng, F. Lai, Z. Li, C. Cheng, L. Zhang, T. Liu, Nano Energy 2021, 81,105622.
- [13] Q. Li, D. Ning, D. Zhou, K. An, D. Wong, L. Zhang, Z. Chen, G. Schuck, C. Schulz, Z. Xu, G. Schumacher, X. Liu, J. Mater. Chem. A 2020, 8, 7733.
- [14] Y.-H. Zhang, D. Zhang, L.-R. Wu, J. Ma, Q. Yi, Z. Wang, X. Wang, Z. Wu, C. Zhang, N. Hu, S.-C. Haw, J.-M. Chen, Z. Hu, G. Cui, Adv. Energy Mater. 2022, 12, 2202341.
- [15] G. Zhang, M. Chen, C. Li, B. Wu, J. Chen, W. Xiang, X. Wen, D. Zhang, G. Cao, W. Li, Chem. Eng. J. 2022, 443, 136434.
- [16] a) B. Li, H. Yan, J. Ma, P. Yu, D. Xia, W. Huang, W. Chu, Z. Wu, Adv. Funct. Mater. 2014, 24, 5112; b) X. Zhong, M. h. Oubla, X. Wang, Y. Huang, H. Zeng, S. Wang, K. Liu, J. Zhou, L. He, H. Zhong, N. Alonso-Vante, C.-W. Wang, W.-B. Wu, H.-J. Lin, C.-T. Chen, Z. Hu, Y. Huang, J. Ma, Nat. Commun. 2021, 12, 3136.
- [17] J. Chen, G. Zou, W. Deng, Z. Huang, X. Gao, C. Liu, S. Yin, H. Liu, X. Deng, Y. Tian, J. Li, C. Wang, D. Wang, H. Wu, L. Yang, H. Hou, X. Ji, Adv. Funct. Mater. 2020, 30, 2004302.
- [18] J. C. Zhang, F. Y. Cheng, S. L. Chou, J. L. Wang, L. Gu, H. Wang, H. Yoshikawa, Y. Lu, J. Chen, Adv. Mater. 2019, 31, 1901808.
- [19] a) A. R. Armstrong, M. Holzapfel, P. Novak, C. S. Johnson, S.-H. Kang, M. M. Thackeray, P. G. Bruce, J. Am. Chem. Soc. 2006, 128, 8694; b) E. Castel, E. J. Berg, M. El Kazzi, P. Novak, C. Villevieille, Chem. Mater. 2014. 26, 5051.
- [20] E. Boivin, N. Guerrini, R. A. House, J. G. Lozano, L. Jin, G. J. Rees, J. W. Somerville, C. Kuss, M. R. Roberts, P. G. Bruce, Adv. Funct. Mater. 2021, 3131, 2003660.
- [21] J. He, G. Melinte, M. S. D. Darma, W. Hua, C. Das, A. Schoekel, M. Etter, A.-L. Hansen, L. Mereacre, U. Geckle, T. Bergfeldt, Z. Sun, M. Knapp, H. Ehrenberg, J. Maibach, Adv. Funct. Mater. 2022, 3232, 2207937.
- [22] R. Baddour-Hadjean, J.-P. Pereira-Ramos, in 22nd Int. Conf. on Raman Spectroscopy, American Institute of Physics, Boston, MA 2010, p. 1137.
- [23] a) R. Baddour-Hadjean, J.-P. Pereira-Ramos, Chem. Rev. 2010, 110, 1278; b) D. Eum, B. Kim, S. J. Kim, H. Park, J. P. Wu, S. P. Cho, G. Yoon, M. H. Lee, S. K. Jung, W. L. Yang, W. M. Seong, K. Ku, O. Tamwattana, S. K. Park, I. Hwang, K. Kang, Nat. Mater. 2020, 19, 419; c) H. C. Guo, Z. Wei, K. Jia, B. Qiu, C. Yin, F. Q. Meng, Q. H. Zhang, L. Gu, S. J. Han, Y. Liu, H. Zhao, W. Jiang, H. F. Cui, Y. G. Xia, Z. P. Liu, Energy Storage Mater. 2019, 16, 220.
- [24] J. Li, H. Hua, X. Kong, H. Yang, P. Dai, J. Zeng, J. Zhao, Energy Storage Mater. 2022, 46, 90.
- [25] a) X. Zhang, J. Zhao, G.-H. Lee, Y. Liang, B. Wang, S. Liu, E. Wang, W. Yang, H. Yu, Adv. Energy Mater. 2023, 13, 2022929; b) J. Zhang, P.-F. Wang, P. Bai, H. Wan, S. Liu, S. Hou, X. Pu, J. Xia, W. Zhang, Z. Wang, B. Nan, X. Zhang, J. Xu, C. Wang, Adv. Mater. 2022, 34, 2108353.





16146840, 2023, 32, Downloaded from https://advanced.onlinelibrary.wiley.com/doi/10.1002/nemm.202301216 by University Town Of Shenzhen, Wiley Online Library on [20/11/2025]. See the Terms

and-conditions) on Wiley Online Library for rules of use; OA articles are governed by the applicable Creative Commons

www.advancedsciencenews.com

www.advenergymat.de

- [26] X. Zhang, J. Zhao, G.-H. Lee, Y. Liang, B. Wang, S. Liu, E. Wang, W. Yang, H. Yu, Adv. Energy Mater. 2023, 13, 2202929.
- [27] a) M. Mao, B. Huang, Q. Li, C. Wang, Y.-B. He, F. Kang, Nano Energy 2020, 78, 105282; b) W. Huang, H. Wang, D. T. Boyle, Y. Li, Y. Cui, ACS Energy Lett. 2020, 5, 1128.
- [28] J. Zhao, X. Zhang, Y. Liang, Z. Han, S. Liu, W. Chu, H. Yu, ACS Energy Lett. 2021, 6, 2552.
- [29] a) F. Wu, W. Li, L. Chen, Y. Su, L. Bao, W. Bao, Z. Yang, J. Wang, Y. Lu, S. Chen, Energy Storage Mater. 2020, 28, 383; b) K. Kim, D. Hwang, S. Kim, S. O. Park, H. Cha, Y.-S. Lee, J. Cho, S. K. Kwak, N.-
- S. Choi, Adv. Energy Mater. 2020, 10, 2000012; c) B. Xiao, H. Liu, N. Chen, M. N. Banis, H. Yu, J. Liang, Q. Sun, T.-K. Sham, R. Li, M. Cai, G. A. Botton, X. Sun, Angew. Chem., Int. Ed. Engl. 2020, 59, 14313.
- [30] W. Huang, C. Lin, J. Qiu, S. Li, Z. Chen, H. Chen, W. Zhao, G. Ren, X. Li, M. Zhang, F. Pan, *Chem* 2022, 8, 2163.
- [31] J. Choi, H. Jeong, J. Jang, A. R. Jeon, I. Kang, M. Kwon, J. Hong, M. Lee, J. Am. Chem. Soc. 2021, 143, 9169.
- [32] Y. Bai, Z. Wang, N. Qin, D. Ma, W. Fu, Z. Lu, X. Pan, Angew. Chem., Int. Ed. 2023, 62, e202303162.